Supplementary information

Visualizing local fast ionic conduction pathways in nanocrystalline lanthanum manganite by isotope exchange-atom probe tomography

Francesco Chiabrera[1,2,†], Federico Baiutti[1,3,†], David Diercks[4], Andrea Cavallaro[5], Ainara Aguadero[5], Alex Morata[1], Albert Tarancón[1,6*]*

(1) Catalonia Institute for Energy Research (IREC), Jardins de Les Dones de Negre 1, 08930 Sant Adrià del Besòs, Barcelona, Spain
(2) Department of Energy Conversion and Storage, Functional Oxides group, Technical University of Denmark, Fysikvej, 310, 233 2800 Kgs. Lyngby, Denmark
(3) Department of Materials Chemistry, National Institute of Chemistry, Hajdrihova 19, Ljubljana SI-1000, Slovenia
(4) Department of Metallurgical and Materials Engineering, Colorado School of Mines, Golden, CO 80401, United States
(5) Department of Materials, Imperial College London, Prince Consort Road, London SW7 2BP, United Kingdom
(6) ICREA, 23 Passeig Lluís Companys, Barcelona 08010, Spain.

[†] *Equal contribution*

[*] *Corresponding author:* fbaiutti@irec.cat, *atarancon@irec.cat*

Supplementary notes

1. FEM simulations

FEM simulations were performed by COMSOL Multiphysics to model the ^{18}O incorporation and diffusion in the grain and grain boundaries (GB) of the LSM thin films. Supplementary **Figure 2a** shows the 2D geometry chosen for the simulations, which was chosen based on the cross section obtained by IE-ATP. The width of the GBs was first set to 1 nm, in accordance with previous works.[1–3] The incorporation of oxygen on the LSM surface was modelled considering a convective-type boundary equation, with two different surface exchange coefficients for the grain and GB surfaces (k^*_g and k^*_{gb}, respectively). The external tracer concentration and the exchange time was set equal to the experimental exchange conditions, while an initial tracer concentration

equal to the natural ^{18}O abundance was considered. In order to reproduce the heterogeneous tracer concentration observed by IE-ATP, two different diffusivity coefficients were set in the grain and GB regions (D^*_g and D^*_{gb}). Time dependent Fick´s second laws of diffusion was then numerically solved by COMSOL Multiphysics. Finally, triangular elements were used for meshing the domains and an element size refinement was performed near the GBs for better characterizing the local concentration gradients, see Supplementary **Figure 2b.**

2. FEM fitting procedure

A parametric sweep of the mass transport coefficients (k^*_g, k^*_{gb}, D^*_g and D^*_{gb}) was performed for achieving a good fitting of the tracer fraction measured by IE-ATP. The initial guessing values were set considering previous publications of oxygen transport in polycrystalline LSM thin films (k^*_g=1.0E-11 cm/s k^*_{gb}=1.0E-9 cm/s, D^*_g=4.0E-17 cm^2/s and D^*_{gb}=4.0E-14 cm^2/s).[1–3] We then performed a set of simulations varying D^*_{gb} from 6.3E-15 to 2.0E-13 cm^2/s (7 values), k^*_{gb} from 1.8E-10 cm/s to 1.8E-8 cm/s (7 values), k^*_g from 1.4E-12 to 1.4E-10 cm/s (3 values) and D^*_g from 2E-18 to 2E-16 cm^2/s (3 values) and calculating all possible the possible combinations (the parameters were equally spaced in logarithmic scale). In this way, the possible interdependence of the mass transport parameters on the FEM fitting could be explored.

We then took advantage of the unique capabilities of IE-ATP of measuring the tracer fraction at the nanoscale and compared the 1D out of plane ^{18}O concentration along the GBs experimentally measured and calculated by FEM simulations (Supplementary **Figure 3**). Here, a selection of profiles calculated in the parametric sweep analysis is shown. In each panel, the results obtained varying k^*_{gb} from 1.8E-9 cm/s to 1.8E-8 cm/s (variation of color) and for D^*_g =1.9E-17 cm^2/s and D^*_g =1.9E-16 cm^2/s (continuous and dashed line, respectively) are depicted. We observed that D^*_{gb} directly relates with the slope of the tracer fraction in the GBs, while k^*_{gb} mainly regulate the

absolute value. The bulk parameters are observed to have a smaller influence on the GB profiles, although a clear variation of the absolute value in the tracer fraction can be observed while varying D^*_g and k^*_g. From this first analysis, we could identify an optimal D^*_{gb} between 9.2E-15 cm^2/s and 4.3E-14 cm^2/s and an optimal k^*_{gb} around 4.0E-10 cm^2/s. GB parameters outside these ranges lead to an unrealistic profile concentration for any value of D^*_g and k^*_g.

We then compared the 1D out of plane ^{18}O concentration measured by IE-ATP along the grain interior and calculated by FEM analysis (Supplementary **Figure 4**). In these simulations, k^*_{gb} was kept constant at 4.0E-10 cm/s and two D^*_{gb}, 2.0E-15 cm^2/s and 4.0E-15 cm^2/s, were considered. The parametric sweep of D^*_g and k^*_g shows that, independently on the GB coefficients, the best fitting is obtained for a D^*_g around 1.0E-17 cm^2/s and k^*_g around 4.5E-12cm/s. It is also possible to note that a single bulk diffusivity is not fully able to reproduce the grain interior tracer profile, pointing at a sub-surface region with a lower diffusivity coefficient (as discussed below).

Finally, we refined the fitting of the GB coefficients by fixing the bulk parameters at the optimal values and by performing a finer parametric sweep of D^*_{gb} and k^*_{gb}. Supplementary **Figure 5** compare the IE-ATP 1D out of plane ^{18}O concentration measured along the GBs with the FEM results. As previously mentioned, D^*_{gb} is primarily responsible of determining the slope of the tracer concentration in the GB region, while k^*_{gb} varies the total concentration of ^{18}O. This analysis was then used to define the best fitting GB transport coefficients and their uncertainties, which was set by the range of D^*_{gb} and k^*_{gb} that allowed a profile within the experimental data scattering. The analysis yield to D^*_{gb} between 1.6E-14 and 4E-14 cm^2/s and k^*_{gb} between 2.6E-14 and 5.1E-10 cm/s, with optimal values of D^*_{gb}=2.1E-14 cm^2/s, k^*_{gb} =4.3E-10 cm/s. This procedure was also used to obtain the uncertainties related to the fitting for the bulk parameters, and is reported in as error bars in **Figure 3** of the main text.

As commented before, the simulations with a single bulk diffusivity coefficients could not yield to a fully satisfactory fitting of the the 1D out of plane ^{18}O concentration in the grain interior (Supplementary **Figure 4**). Here, two different slopes appears in the tracer profile, very steep in the first 5 nm and more flat in the other part of the film. We note that this effect cannot be related with a porosity of the surface, since no drastic decrease of the cationic composition is observed (as it would be expected in the case of prosity/cracks, **Figure 4** of the main text). On the contrary, the rapid increase of Sr observed in this region suggest a segregation of the dopant, as commonly observed in perovskites. The change of subsurface composition inspired us to develop another model, with the very same geometry of the previous one but a different bulk diffusivity coefficient in the first 5 nm ($D^*_{g,s}$). We then performed a parametric sweep of $D^*_{g,s}$ and D^*_g, leaving all other parameters with the optimized value obtained in the previous analysis. As shown in Supplementary **Figure 6**, an improvement of the fitting in the grain interior is clearly observed for D^*_g=1.0E-16 cm^2/s and $D^*_{g,s}$=1.5E-17 cm^2/s. It is important to note that the additional parameter did not vary substantially the GB profiles, which could be reproduced with the exact same parameters.

3. FEM model of space charge scenario

It was recently proposed by Börgers et al. that fast diffusivity along dislocations in LSM thin films is a space charge phenomenon, where oxygen vacancies accumulate in the dislocation surroundings to compensate a negatively charged dislocation core.[4] We therefore developed a space charge FEM model to verify if the IE-ATP tracer distribution could be ascribed to a fast diffusion along the space charge region and not in the core. The model is based on the presence of a 0.5 nm internal core with diffusivity equal to the bulk region (D_g) and a space charge area with diffusivity (D_{sc}) described by an error function type equation,[5] as:

$$D_{sc} = D_g + (D_{gb} - D_g)\bullet(1 + erf(\pm(x - x_{gb})/\gamma) \quad \text{Eq. S1}$$

With x_{gb} equal to the GB core position and γ defying the space charge width. The equation was applied symmetrical to the GB core, with a plus sign in the erf defying the negative x direction and a minus sign the positive one. The error function equation was chosen to describe the extent of the diffusivity increase (*i.e*. oxygen vacancy accumulation) since the exact solution of the space charge is still unknown for LSM. Supplementary **Figure 7a** shows the color map of the oxygen diffusivity variation considered in the simulations, while Supplementary **Figure 7b** shows the 1D distribution of diffusivity across a GB. The increase of surface exchange coefficient in the GB region was also described by Eq. S1, substituting D^*_{gb} and D^*_g by k^*_{gb} and k^*_g, respectively (see Supplementary **Figure 7c**). The fitting procedure was performed in the same fashion as described in the previous section, by performing a large parametric sweeps analysis. γ was fixed to 0.3 nm.

Supplementary **Figure 8** shows the comparison between the 2D tracer contours of the simulations obtained with a fast core diffusivity and with the space charge model. In the latter, the fitting procedure yield to the following oxygen transport parameters: D^*_{gb}=1.5E-14 cm^2/s, k^*_{gb} =3.8E-10 cm/s, k^*_g =4.5E-12cm/s D^*_g=1.0E-16 cm^2/s and $D^*_{g,s}$=1.5E-17 cm^2/s. We note that these values are very close to the ones obtained in the simulations with fast core diffusivity. Indeed, the 2D contour plots and the 1D horizontal ^{18}O fraction profiles obtained with the two different models are very similar. The main difference is the width of the maximum tracer concentration at the grain boundary, larger in the space charge model due to a larger volume of enhanced diffusivity. We also note that the 0.5 nm core present a flat tracer concentration, meaning that the bulk diffusivity of LSM is enough for allowing a fast diffusion within this limited length. Overall, the results shows that the both model are able to reproduce the IE-APT tracer distribution in polycrystalline LSM thin films.

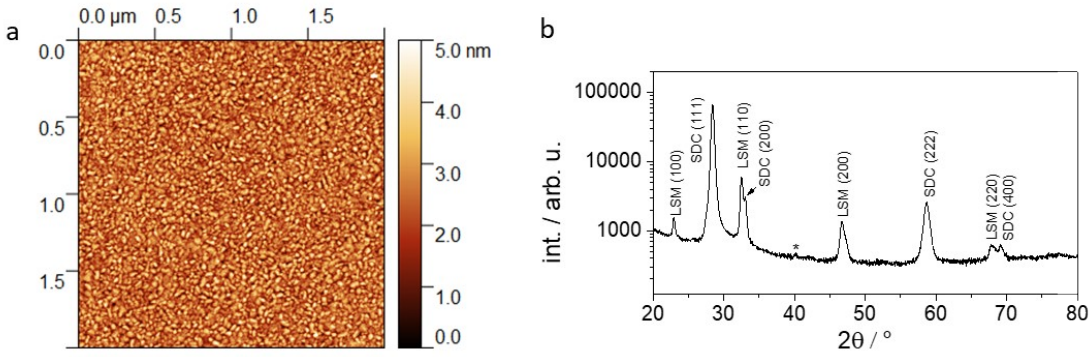

Supplementary Figure 1. a, Atomic Force Microscopy topography of the LSM thin films showing a fully dense structure with nanometric grain size. b, X-Ray Diffraction patterns of the LSM/SDC bilayers on Al_2O_3 (0001) single crystals. The asterisk (*) indicates the position of the substrate peak.

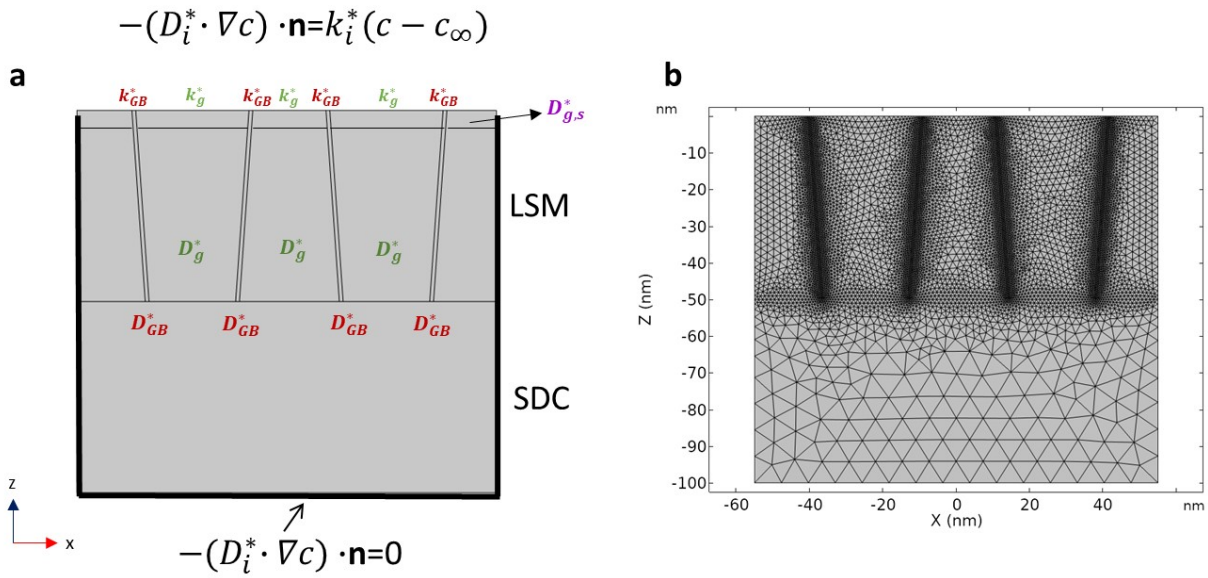

Supplementary Figure 2. a, Geometry, parameters and main boundary conditions adopted in the FEM simulations. b, Optimized mesh adopted in the simulations.

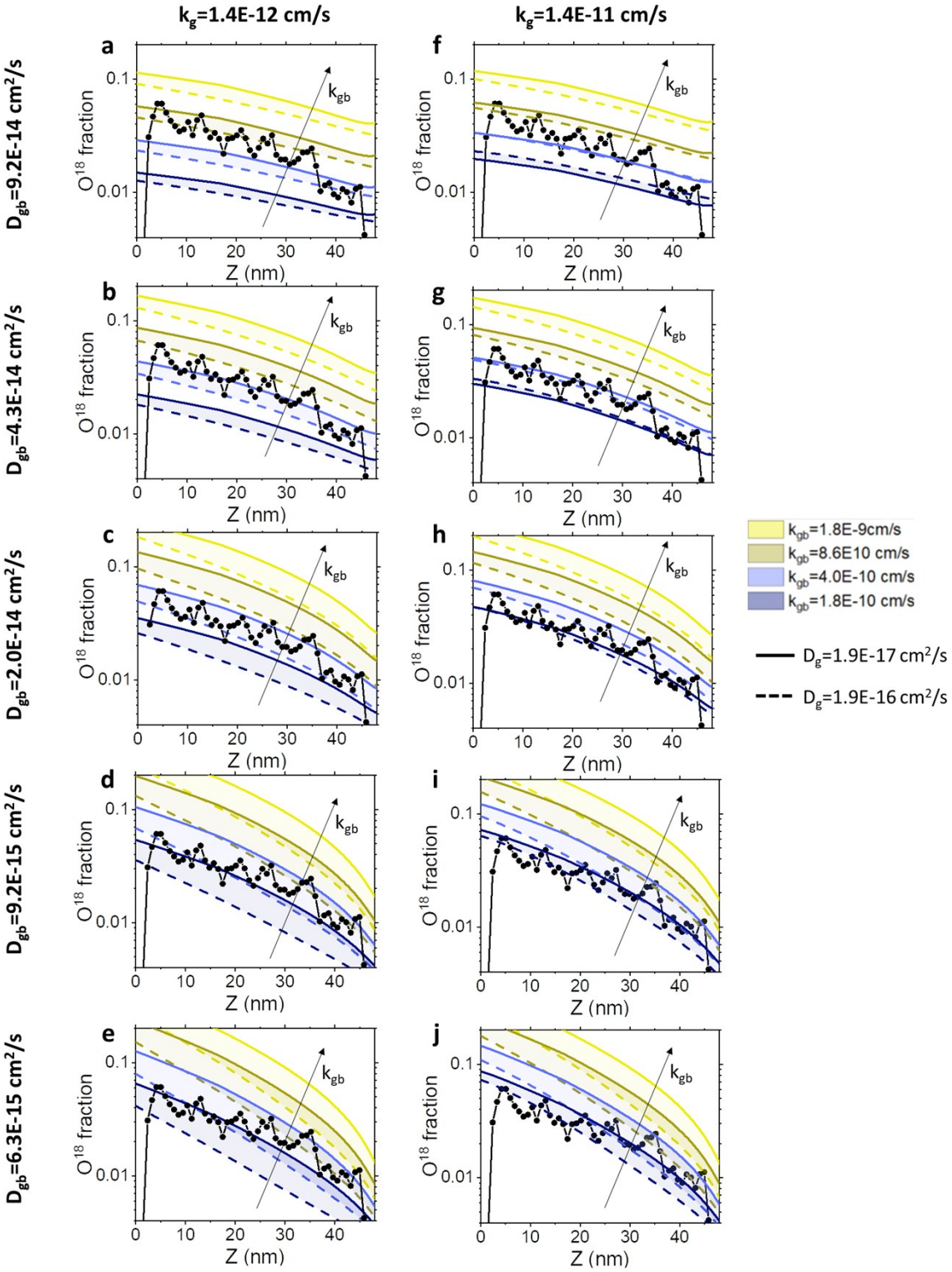

Supplementary Figure 3. Out-of-plane tracer fraction measured by IE-ATP along the GB region and calculated by the FEM simulation for a variety of transport coefficients (k^*_g , k^*_{gb},, D^*_g and D^*_{gb}). The results obtained for two different k^*_g and four D^*_{gb} are shown in the different panels. In each panel, k^*_{gb} is varied from 1.8E-10 cm/s to 1.8E-10 cm/s. Also, two different D^*_b are considered, depicted as dashed and continuous lines (1.9 E-16 cm2/s and 1,9E-17cm2/s, respectively).

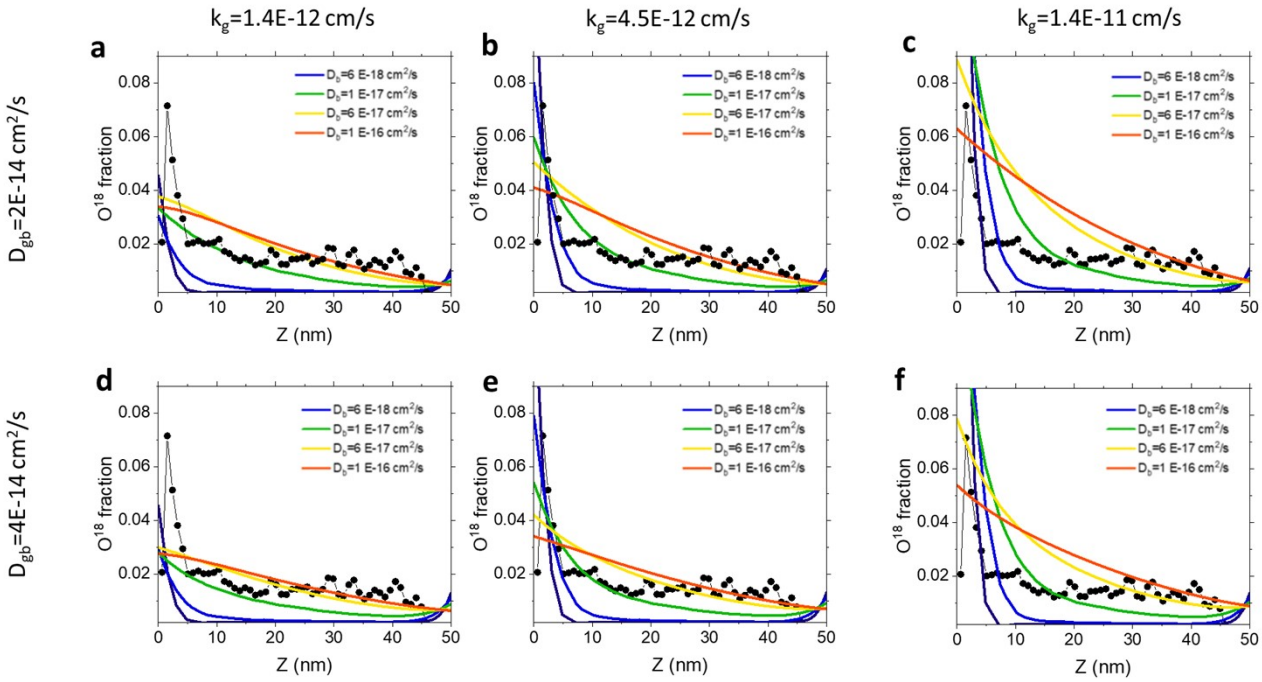

*Supplementary Figure 4. Out-of-plane tracer fraction measured by IE-ATP along the grain interior and calculated by the FEM simulation for a variety of bulk transport coefficients (k^*_g, D^*_b). The results obtained for two different D^*_{gb} are shown **a-c** (2E-14cm²/s) and **d-f** (4E-14cm²/s), while k^*_g is kept at 4E-10c cm/s. In each panel, D^*_g is varied from 6.0E-18 cm²/s to 1.0E-16 cm²/s.*

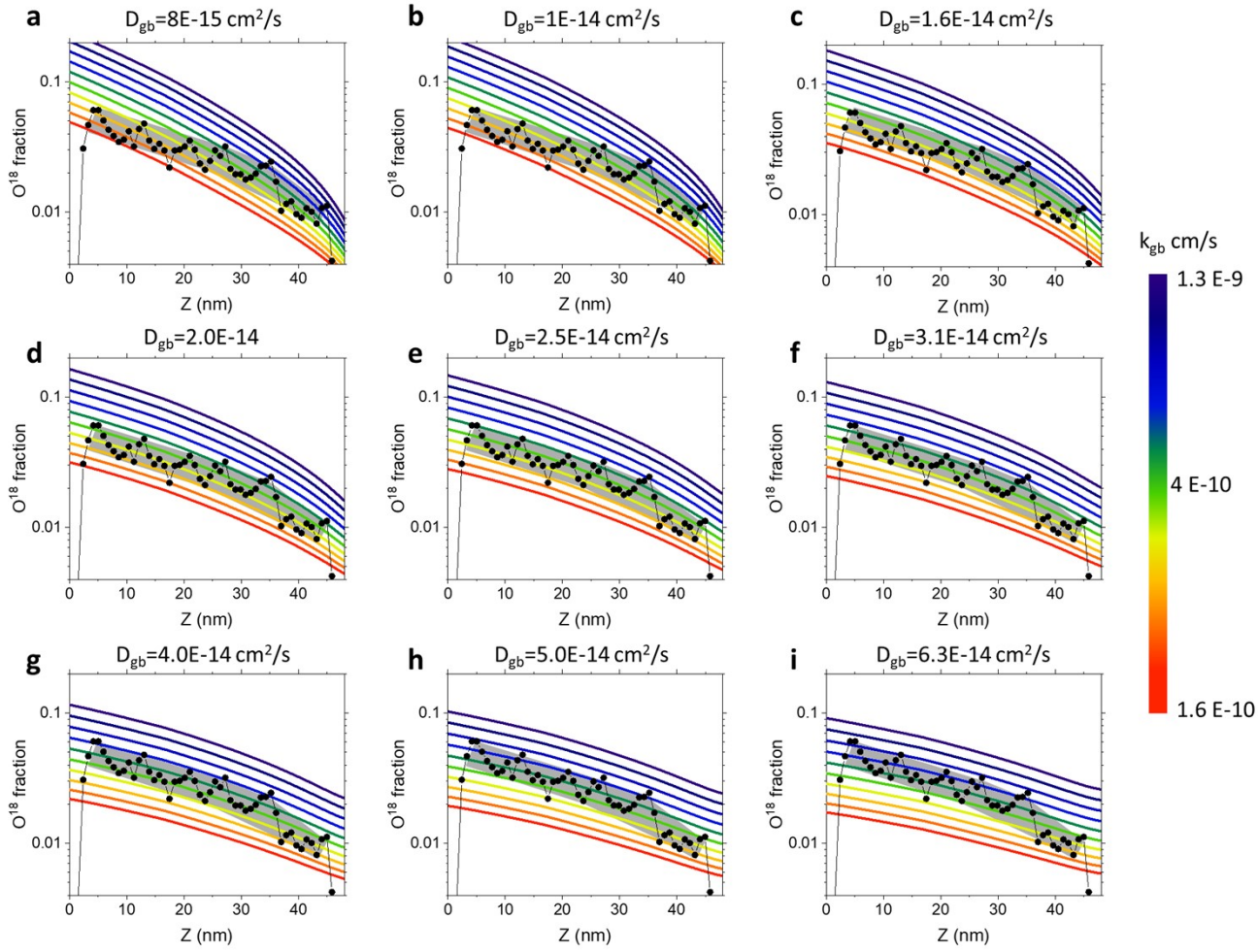

Supplementary Figure 5. Out-of-plane tracer fraction measured by IE-ATP along the GB region and calculated by the FEM simulation for a variety of GB transport coefficients (k^*_{gb},, and D^*_{gb}). In the simulations, D^*_g is kept at 1.0E-17 cm²/s and k^*_g at 4.5E-12cm/s. The grey region in each panel shows the scattering of the experimental data and it is used for determining the error bars in the GB parameters of Figure 3 of the main text.

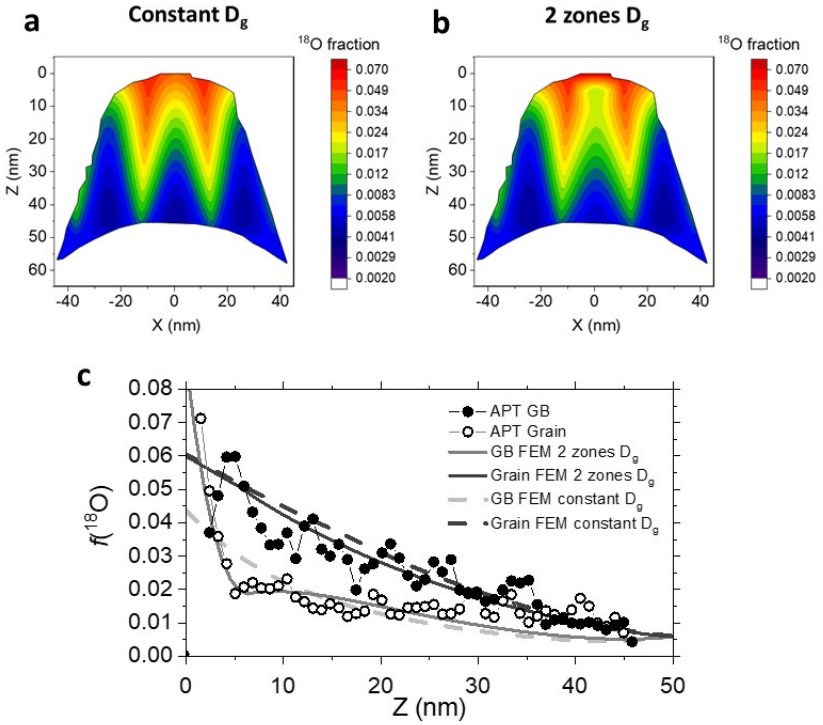

Supplementary Figure 6. Comparison between the ^{18}O fractions obtained in the FEM model with constant bulk diffusivity (a) and in the model with a slower subsurface diffusivity (b, in the first 5 nm). All other parameters are kept fixed in the two simulations. c, 1D out-of-plane profiles of the 18O fraction simulated along the GB and along the grain bulk for the two different models. The 2 zones model improves the resemblance with the experimental results in the subsurface region of the grain bulk. No major differences are observed in the two model for the GBs.

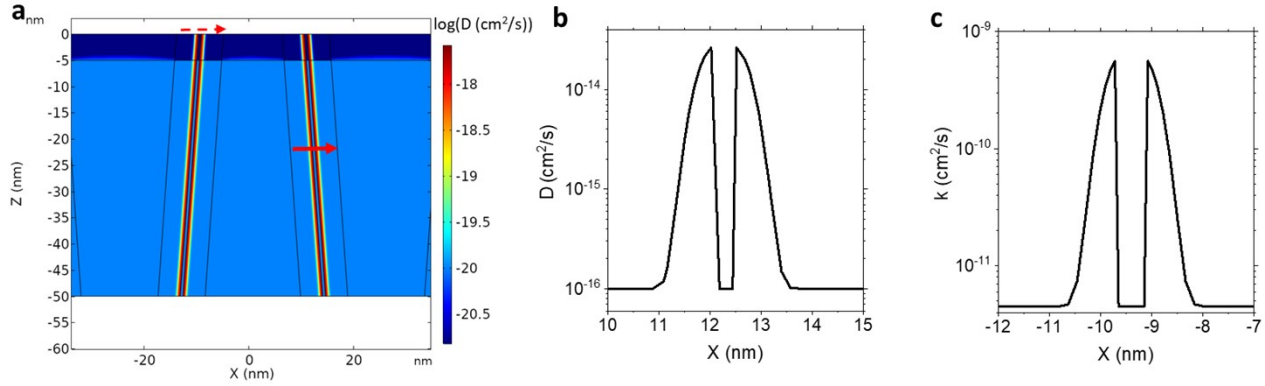

*Supplementary Figure 7. **a,** 2D distribution of diffusivity used in the space charge model. **b**, 1D diffusivity profile obtained by the Equation S1 across the GB highlighted by the continuous red line in **a** (D^*_g=1.0E-16 cm²/s, D^*_{gb}=2.0E-14 cm²/s and γ=0.3 nm). **c**, 1D surface exchange coefficient profile obtained by the Equation S1 across the GB highlighted by the dashed red line in **a** (k^*_g=4.5E-10 cm/s, k^*_{gb}=3.8E-10 cm/s and γ=0.3 nm).*

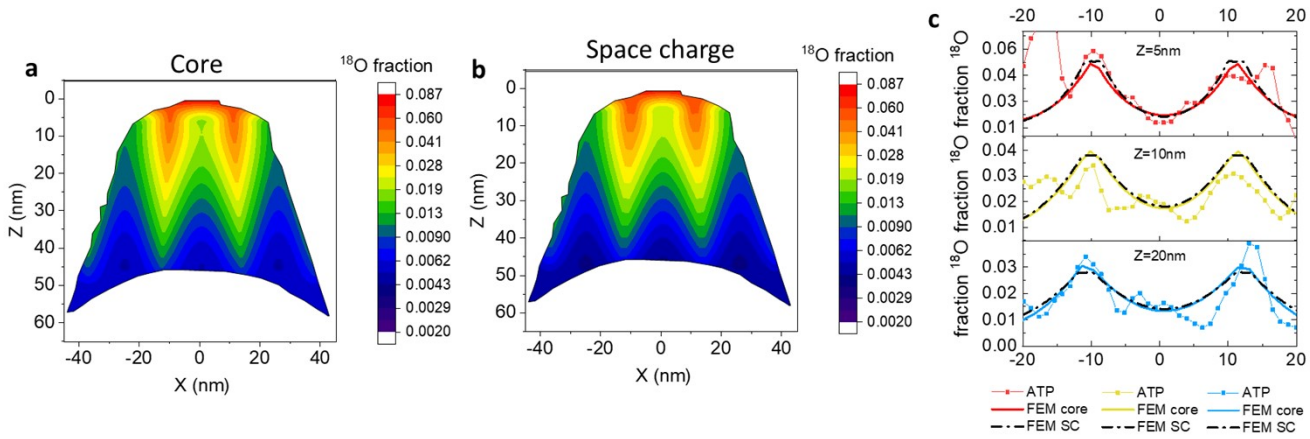

*Supplementary Figure 8. Comparison between the ^{18}O fractions contours obtained in the fast core diffusivity model (**a**) and in the space charge model (**b**).**c,** 1D horizontal profiles of the ^{18}O fraction measured at different distances from the sample's surface and calculated by the two different FEM models.*

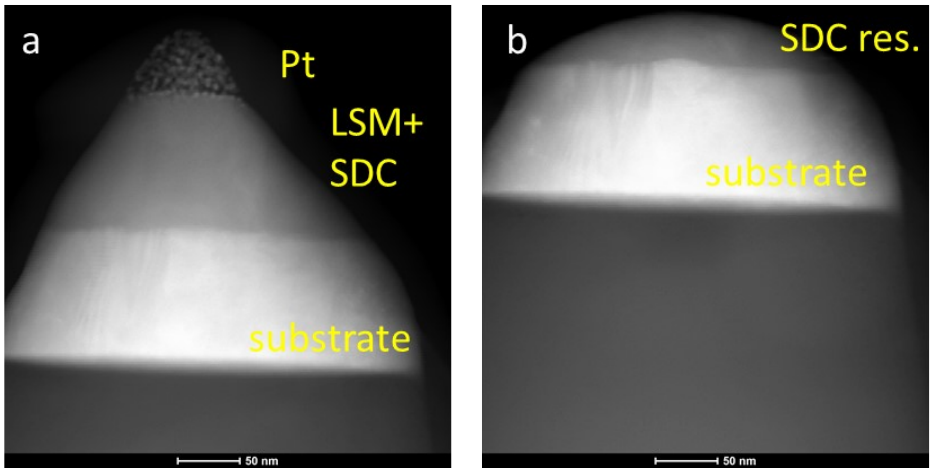

Supplementary Figure 9. STEM-HAADF image of a nanocrystalline LSM thin film APT specimen before APT analysis (a). At the top of the specimen is residual electron-beam deposited Pt from the specimen preparation. The layer below that is the LSM; then the ceria buffer layer and Al_2O_3 substrate. The figure on the right is the same specimen after APT analysis (b).

Supplementary references

1 A. M. A. M. Saranya, A. Morata, D. Pla, M. Burriel, F. Chiabrera, I. Garbayo, A. Hornés, J. A. J. A. Kilner and A. Tarancón, *Chem. Mater.*, 2018, **30**, 5621–5629.

2 E. Navickas, T. M. Huber, Y. Chen, W. Hetaba, G. Holzlechner, G. Rupp, M. Stöger-Pollach, G. Friedbacher, H. Hutter, B. Yildiz and J. Fleig, *Phys. Chem. Chem. Phys.*, 2015, **17**, 7659–7669.

3 F. Baiutti, F. Chiabrera, D. Diercks, A. Cavallaro, L. Yedra, L. Lopez-Conesa, S. Estradé, F. Peiró, A. Morata, A. Aguadero and A. Tarancon, *Adv. Mater.*, , DOI:10.1002/adma.202105622.

4 J. M. Börgers, J. Kler, K. Ran, E. Larenz, T. E. Weirich, R. Dittmann and R. A. De Souza, *Adv. Funct. Mater.*, 2021, **2105647**, 1–8.

5 R. A. De Souza, C. Voisin, H. Schraknepper, M. Teusner, M. Kessel, P. Dufour, C. Tenailleau and S. Guillemet-Fritsch, *Phys. Chem. Chem. Phys.*, 2014, **16**, 2568–2575.